Journal of
Materials Chemistry A

PAPER

View Article Online
View Journal | View Issue

Cite this: *J. Mater. Chem. A*, 2022, **10**, 4209

Remarkable CO_x tolerance of Ni^{3+} active species in a Ni_2O_3 catalyst for sustained electrochemical urea oxidation†

Muhammed Safeer N. K.,[ab] Chandraraj Alex,[a] Rajkumar Jana,[c] Ayan Datta[c] and Neena S. John*[a]

Received 7th July 2021
Accepted 4th January 2022

DOI: 10.1039/d1ta05753g

rsc.li/materials-a

The electrochemical urea oxidation reaction (UOR) provides a cost-effective way of generating hydrogen owing to its low thermodynamic energy barrier. Although the UOR is an effective way to generate hydrogen, sustained activity and long-term catalyst usage are retarded by CO_x poisoning. In nickel oxide-based UOR electrocatalysts, enhancing Ni^{3+} active species (NiO(OH)) is one of the effective ways to improve the activity. In this study, we show that Ni_2O_3 is a promising UOR catalyst with Ni^{3+} ions being highly active and the UOR activity is seen to be almost six times higher than that of NiO. Ni_2O_3 shows retention of 70% UOR performance even after 25 hours at an average current density of 25 mA cm^{-2}, whereas the NiO system loses 50% of its activity within 10 h even at a low current density of 5.1 mA cm^{-2}. The efficient and sustained UOR activity of Ni_2O_3 can be correlated with the highly tolerant Ni^{3+} ions in the Ni_2O_3 system towards CO_x poisoning compared to the tolerance of NiO, as proved by impedance studies. The impedance spectra acquired at various applied potentials in the UOR regime show a highly significant reverse loop (real impedance is negative) for NiO indicative of impeding CO_x desorption as a rate-determining step in the 0.48 to 0.52 V potential window, whereas for Ni_2O_3, it is less influential under the same conditions indicating the better tolerance of Ni_2O_3 towards CO_x poisoning. Furthermore, this is reflected in the fast electro-oxidation kinetics of Ni_2O_3 with a lower Tafel slope value (21 mV dec^{-1}) than NiO (104 mV dec^{-1}). The higher CO_x tolerance of the Ni_2O_3 catalyst is the main reason behind the remarkable stability of the catalyst. Theoretical modeling supports the high activity of Ni_2O_3 through effective adsorption of reactants such as urea and hydroxide with feasible CO_2 removal on the Ni_2O_3 surface.

Introduction

Hydrogen production from water electrolysis holds a clear advantage of using the earth-abundant source of water resources; however, it suffers from the requirement of high potential for the counter water oxidation reaction (1.23 V *vs.* RHE).[1] The higher overpotential for water oxidation or the oxygen evolution reaction (OER) seriously affects the efficiency of hydrogen production and has a huge bearing on commercialization.[2] The requirement of high applied potential for hydrogen production can be dramatically reduced by replacing the OER with the urea electro-oxidation reaction (UOR). Urea is a waste product, abundantly available in human and animal urine and it is also present in sewage. In the year 2010, approximately 2000 billion tons of wastewater was generated worldwide and most of it has flowed into other water bodies.[3] The human body generates on average 20–30 mg of urea in a day.[4] UOR and urea-based fuel cells have gained a lot of importance recently, facilitating waste water purification combined with energy generation. Nickel-based catalysts are extensively used for the UOR in alkaline medium as nickel oxyhydroxide (NiO(OH)) is shown to be the active intermediate. Vedharathinam *et al.* have proven mechanisms for urea electro-oxidation using *in situ* Raman spectroscopy.[5,6] The overall reaction scheme and cell potential involved in hydrogen production are given below.

Anode:

$$CO(NH_2)_2 + 6OH^- \leftrightarrow N_{2(g)} + 5H_2O + CO_{2(g)} + 6e^-, (E^0_{ox.} = -0.46\ V\ vs.\ SHE) \quad (1)$$

Cathode:

$$6H_2O + 6e^- \leftrightarrow 6OH^- + 3H_{2(g)}, (E^0_{red} = -0.828\ V\ vs.\ SHE) \quad (2)$$

---

[a] Centre for Nano and Soft Matter Sciences (CeNS), Shivanapura, Bengaluru 562162, India. E-mail: jsneena@cens.res.in

[b] Manipal Academy of Higher Education, Manipal 576104, India

[c] School of Chemical Sciences, Indian Association for the Cultivation of Science (IACS), Kolkata 700032, India

† Electronic supplementary information (ESI) available. See DOI: 10.1039/d1ta05753g

Overall:

$$CO(NH_2)_2 + H_2O \rightarrow N_{2(g)} + 3H_{2(g)} + CO_{2(g)}, (E^0_{cell} = -0.37\ V\ vs.\ SHE) \quad (3)$$

Urea electrolysis requires only a potential of −0.37 V *vs.* SHE for the generation of H_2. Nickel oxide and hydroxide-based nanomaterials have been employed for the electrochemical UOR in previous studies. Most of the earlier studies have been focused on improving the catalyst activity. The sustained activity of the catalyst for a longer duration is challenging.[7] Guo *et al.* synthesized Ni nanowires by electrodeposition. They measured the stability in 5 M KOH containing 0.33 M urea, and a rapid current density decrease from 140 mA cm^{-2} to 50 mA cm^{-2} within 0.5 h is noticed due to the occupation of gaseous intermediates on the active site of the catalyst.[8] Hameed *et al.* have studied the stability of nickel oxide deposited on various substrates, and NiO deposited on a graphite substrate[9] has shown stability for 0.5 h at a current density of 6.67 mA cm^{-2}. In the case of carbon fiber incorporated NiO, UOR activity shows a current degradation from 30 to 19.99 mA cm^{-2} in a concise duration of 800 seconds,[10] indicating the possibility of catalyst poisoning. Very recently, in 2021, Lu *et al.*[11] have studied the UOR activity of nano-nickel oxide in eggshell membrane-derived carbon, which shows an initial current density of 0.05 mA cm^{-2} that degraded to 0.015 mA cm^{-2} in 0.5 h. A nickel oxide–nickel hybrid nanoarray on nickel foam has been studied for the electrochemical UOR by Yue *et al.*[12] and has shown 16 h stable catalytic activity at a current density of 10 mA cm^{-2}. Zhang *et al.*[13] synthesized Ni^0 rich Ni/NiO by acid etching followed by (H_2/Ar) annealing. The above catalyst has shown a superior activity towards the UOR with minimal degradation in 50 mA cm^{-2} (current density) up to 20 h at a potential of 1.62 V. In many reports, higher current density for the UOR is obtained only when the catalyst is loaded on nickel foam, which itself is UOR active.

The challenge in sustained catalyst activity and stability is explained mainly due to catalyst surface poisoning by the adsorption of reaction intermediates such as NCO^-, CO_2, and others. Among these intermediates, the potential poison that causes severe degradation in the activity is CO_2.[14] The catalyst poison leads to the unavailability of active catalytic sites for further reaction and shortens the catalyst life span. Very recently, from our group, Alex *et al.*[15] reported the importance of surface defects and effective removal of adsorbed catalyst poisons for improving electrochemical urea oxidation. They have observed that strong urea adsorption on defective NiO leads to higher catalytic surface poisons favoring the direct UOR and can be removed by adjusting the urea and KOH ratio. In search of a better nickel oxide-based catalyst with a higher number of active species (NiO(OH)) that can tolerate CO_x poisons, we investigated the Ni_2O_3 system for the UOR and compared it with NiO. To the best of our knowledge, Ni(III)oxide has not been reported for the UOR application previously. Both the catalysts have Ni^{3+} active species (NiO(OH)) on their surface with Ni_2O_3 possessing higher Ni^{3+} active species providing effective interaction with urea and hydroxyl. A combination of voltammetry and impedance studies in various UOR potential regimes and at different urea–KOH electrolyte concentrations is performed to have a better understanding of the influence of CO_x poisons in both cases. The impedance study reveals the presence of less significant surface oscillatory phenomena with negative real impedance values for Ni_2O_3 indicative of CO_x poisoning to a lesser extent. The excellent CO_x removal comes from effective OH^- ion adsorption and its surface saturation on Ni_2O_3 samples, whereas NiO has poor OH^- adsorption. The high CO_x tolerance of the active species on the Ni_2O_3 surface is correlated with the superior stability of UOR activity up to 25 h at an average current density of 25 mA cm^{-2} in dilute urea solution (0.150 M urea in 1 M KOH). The effective interaction of urea and hydroxyl with the Ni_2O_3 surface and weak CO_2 interaction are supported by density functional theory (DFT) calculations.

Experimental details

Synthesis of NiO and Ni_2O_3

Nickel hydroxide was precipitated by adding 5 mL of 0.92 g of KOH (Merck) to a solution containing 2.48 g of $NiNO_3 \cdot 6H_2O$ (SDFCL) in 25 mL of ultra-pure (type 1) water. The solution is heated to 90 °C for 1 h. The obtained green color precipitate was washed with DI water and ethanol several times to remove unreacted nickel nitrate impurities, and finally, the green $Ni(OH)_2$ powder was dried at 90 °C.[16] The obtained $Ni(OH)_2$ powder was annealed at 400 °C in air for 1 h at a heating rate of 5 °C per minute to obtain black NiO powder.[17]

Nickel nitrate was oxidized directly to obtain Ni_2O_3. We have synthesized Ni(III)oxide using a precipitation method with slight modification to the synthesis reported by Dey *et al.*[18] 2.48 g of $NiNO_3 \cdot 6H_2O$ was dissolved in 25 mL of water (type 1) and NaClO (4% w/v available chlorine, Merck) is added dropwise to this solution under magnetic stirring at 500 rpm under ambient conditions until the solution completely turns black. The reaction was kept for 1 h and the obtained precipitate was washed with DI water followed by drying in an oven at 90 °C for 1 h.

Characterization techniques

X-ray diffraction (XRD) analyses were performed using a Rigaku SmartLab diffractometer with $Cu_{K\alpha}$ incident radiation (40 kV and 30 mA) from nickel oxide powder. Raman spectra were acquired using a HORIBA XploRA PLUS confocal Raman microscope using a 532 nm excitation laser (10% laser power) with an acquisition time of 30 seconds. A field emission scanning electron microscope (FESEM) (TESCAN MIRA3 LM, Brno, Czech Republic) operated at 10 kV with an attached Bruker Nano XFlash 6|30 was used to study the surface morphology and perform energy dispersive spectroscopy (EDS). XPS measurements were carried out with an Omicron ESCA+ integrated with dual-beam charge neutralization. A high-resolution transmission electron microscope (HRTEM, TALOS F200S G2, Thermo Fisher Scientific) operated at 200 kV was used to perform further structural and morphological characterization and electron diffraction.

Electrochemical measurements

All electrochemical measurements were performed using a CHI 760 E electrochemical workstation with a three-electrode setup. 2 mg of the catalyst (NiO or Ni_2O_3) was dispersed in a solution containing a 200 μL isopropyl alcohol–water (type 1) mixture (1 : 3 ratio) along with 50 μL (1 wt%) of Nafion solution by sonication for 2 h to obtain a homogeneous catalyst ink. 5 μL of the above solution was drop-cast onto a previously cleaned glassy carbon electrode (GCE) of diameter 0.07 cm^2 and used as the working electrode. A Pt spring and $Ag/AgCl_{(sat.KCl)}$ are used as the counter and reference electrodes, respectively. Cyclic voltammetry (CV) was performed at various scan rates in the potential window of −0.2 V to +0.65 V *vs.* $Ag/AgCl_{(sat.KCl)}$ in mixtures of urea–KOH solutions as the electrolyte. The concentrations of KOH (Merck) and urea (Merck) are varied for each catalyst to obtain the best solution for electrochemical urea oxidation. Electrochemical impedance spectroscopy (EIS) was performed in a frequency range of 10^5 to 10^{-2} Hz. Before capturing the impedance data, an equilibration time of 180 s was allowed for the system at each polarization potential. The amplitude of the sinusoidal wave was set to 5 mV. Amperometric measurements were done in a 6 M KOH electrolyte solution containing 0.150 M urea at a potential of 0.40 V *vs.* $Ag/AgCl_{(sat.KCl)}$ for the NiO catalyst. The stability of the Ni_2O_3 catalyst was monitored at a potential of 0.58 V *vs.* $Ag/AgCl_{(sat.KCl)}$ in a 1 M KOH electrolyte solution containing 0.150 M urea. The initial current density during chronoamperometry was verified to match the current density obtained for the linear sweep voltammogram (LSV) at that particular potential and pH. The electrochemical stability of the catalyst was performed using an L-shaped GCE (surface area 0.07 cm^2) for feasible removal of the gaseous products of the UOR during a 25 h run.

Results and discussion

The crystal structures of the synthesized systems NiO and Ni_2O_3 have been verified by XRD. The XRD peaks obtained at 37.2°, 43.3°, 62.9°, 75.4° and 79.4° correspond to the planes (111), (200), (220), (311) and (222), respectively, of NiO as shown in Fig. 1(a). These diffraction peaks are in perfect agreement with the face-centered cubic (FCC) structure of NiO (JCPDS no. 075-0269). The XRD pattern of the as-obtained black shiny powder sample of Ni_2O_3 is presented in Fig. 1(b). Diffraction peaks observed at 27.5°, 31.8°, 45.6°, 56.6° and 66.3° could be indexed to (101), (002), (111), (202) and (004) planes corresponding to hexagonal Ni_2O_3 (JCPDS no. 014-0481). Additionally, broad peaks corresponding to the (001) and (101) planes of $Ni(OH)_2$ are also observed in the case of the synthesized Ni_2O_3. It has been reported by Fingerle *et al.*[19] that the high oxidation state of Ni^{3+} ions is feasible to undergo surface reduction to a lower oxidation state of Ni^{2+} ions. This unstable nature of Ni^{3+} ions leads to the formation of $Ni(OH)_2$. The simulated XRD patterns of the corresponding compounds from the JCPDS files are shown just below the obtained diffraction patterns (Fig. 1(a) and (b)). The Raman spectra of the synthesized systems, NiO and Ni_2O_3, are shown in Fig. S1.† The two broad peaks observed around 515 and 1075 cm^{-1} belong to the longitudinal one phonon (1P) and two phonon (2P) modes due to Ni–O vibrations.[20]

The morphology of the nickel oxides is examined using FESEM and TEM. Fig. S2† shows the SEM image of NiO crystallites and a magnified image of the same shows that NiO crystallites have an approximate diameter in the range 10–70 nm. In comparison, Ni_2O_3 has an agglomerated sheet-like morphology (Fig. 2(c)). A similar but clear image of the NiO crystallites and Ni_2O_3 sheets is observed under TEM (Fig. 2(a) and (d)) as well. Fig. 2(b) shows the high-resolution TEM (HRTEM) image of a NiO crystallite with well-defined lattice

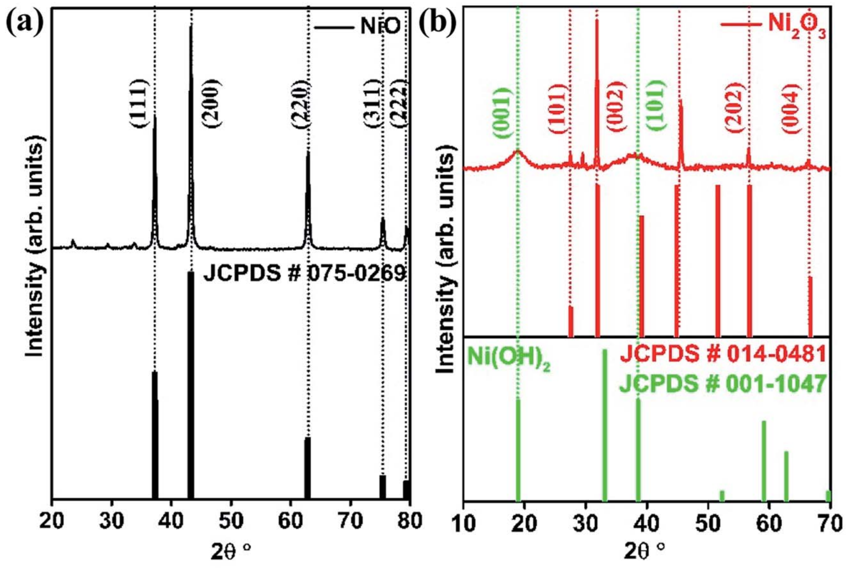

Fig. 1 XRD pattern of (a) NiO and (b) Ni_2O_3.

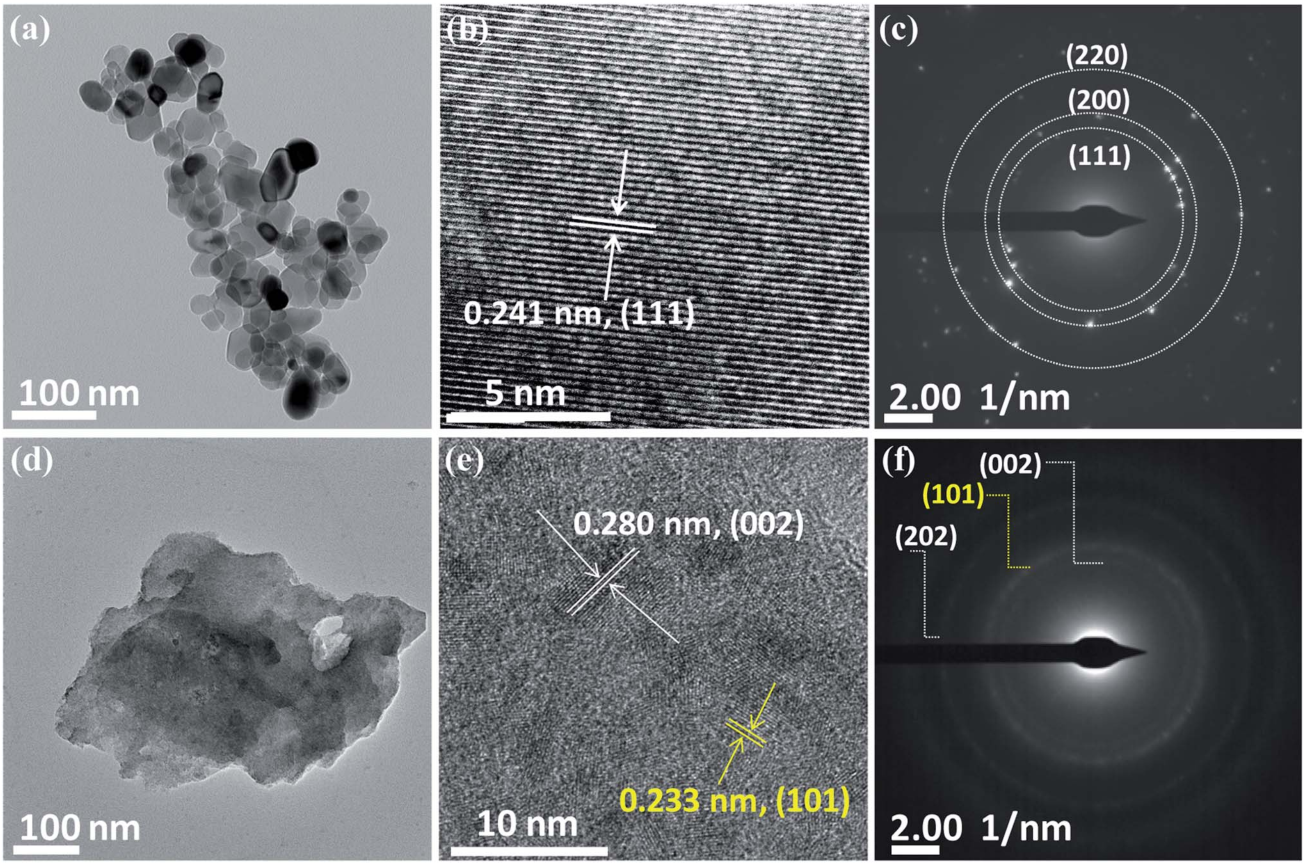

Fig. 2 TEM images of NiO (a–c) and Ni_2O_3 (d–f). (a) NiO crystallites, (b) HRTEM of NiO, (c) SAED pattern of NiO and (d) Ni_2O_3 sheets, (e) HRTEM of Ni_2O_3 sheets and (f) SAED pattern of Ni_2O_3 sheets (HRTEM and SAED of $Ni(OH)_2$ are highlighted in yellow color).

fringes analogous to the (111) plane with an interplanar spacing distance of 0.241 nm. Lattice fringes are visible for Ni_2O_3 and are shown in Fig. 2(e) with an interlayer spacing of 0.280 nm corresponding to the (002) plane. The lattice fringes of the (101) plane belonging to $Ni(OH)_2$ are identified by TEM and support the presence of $Ni(OH)_2$ in accordance with the observation from XRD. The selected area electron diffraction (SAED) pattern of NiO shows planes such as (111), (200) and (220) corresponding to NiO (Fig. 2(c)), whereas Ni_2O_3 gives the (002) and (202) planes of Ni_2O_3, along with the (101) plane of $Ni(OH)_2$ (Fig. 2(f)). A uniform distribution of the constituents, nickel and oxygen for both the prepared samples is confirmed by elemental mapping in TEM (Fig. S3†).

XPS measurements are carried out to examine the surface chemical composition of the as-synthesized nickel oxides. The XPS survey spectra of NiO and Ni_2O_3 are given in Fig. S4.† Fig. 3(a) shows the Ni $2p_{3/2}$ and Ni $2p_{1/2}$ spin–orbit splitting of NiO and Ni_2O_3 samples. The Ni $2p_{3/2}$ component of NiO can be deconvoluted into peaks contributed by Ni^{2+} and Ni^{3+} states, which are located at 853.4 and 855.5 eV.[21] Similarly, peaks due to Ni^{2+} and Ni^{3+} states can be discerned from Ni $2p_{1/2}$ with a binding energy of 871.1 and 873.2 eV, respectively. The satellite peaks of NiO are represented as Sat1 and Sat2 with a binding energy of 860.9 and 879.0 eV. Similarly, the Ni $2p_{3/2}$ and Ni $2p_{1/2}$ peaks of the Ni_2O_3 sample are deconvoluted into peaks due to Ni^{2+} and Ni^{3+} located at binding energies of 854.1 and 855.8 eV ($2p_{3/2}$) and 871.9 and 873.7 eV ($2p_{1/2}$), respectively. The satellite peaks from Ni_2O_3 are observed at 861.4 and 879.6 eV. The presence of Ni^{2+} peaks in Ni_2O_3 further indicates the formation of NiO or hydroxide arising from surface reduction.

We have also calculated the ratio of Ni^{3+}/Ni^{2+} from the deconvoluted spectra of NiO and Ni_2O_3. A higher Ni^{3+}/Ni^{2+} intensity ratio of 2.07 was noticed for Ni_2O_3 as compared to NiO ($Ni^{3+}/Ni^{2+} = 1.36$). The O 1 s spectra, along with their deconvoluted peaks, are displayed in Fig. 3(b). The O 1s peak from NiO is deconvoluted into two peaks: O_1 at 529.3 eV and O_2 situated at 531.3 eV. The intense peak O_1 is attributed to O^{2-} from the Ni–O lattice.[22] The O_2 peak at higher binding energy indicates surface adsorbed oxygen (O_2), which belongs to defective sites.[23,24] Similarly, the O 1s peak of Ni_2O_3 samples can be deconvoluted into three peaks: O_1 (lattice oxygen) at a lower binding energy value of 529.4 eV, O_2 (defect state) observed as a broader peak at 531.3 eV and the O_3 peak at 531.5 eV (hydroxide from $Ni(OH)_2$).[25,26] The percentage of lattice oxygen (O_1), adsorbed oxygen (O_2) and hydroxide (O_3) are given in Table S2.† The EDS study shows that Ni_2O_3 has a high O/Ni ratio of 3.48, which is 1.48 in the case of NiO and supports the presence of a high oxygen content in Ni_2O_3 (Table S1†).

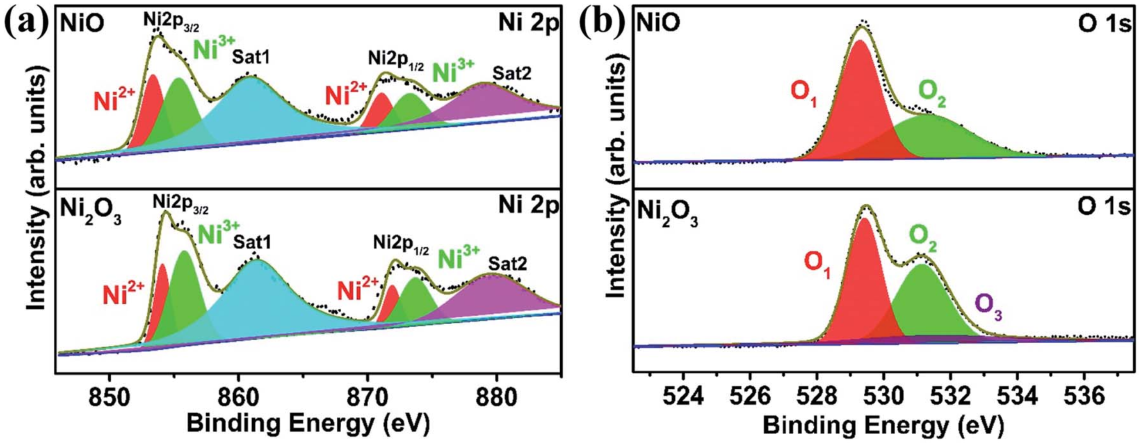

Fig. 3 High-resolution XPS of NiO and Ni_2O_3: (a) Ni 2p spectra and (b) O 1s spectra.

Electrochemical studies

GCEs modified with NiO and Ni_2O_3 are studied for electrochemical urea oxidation employing cyclic voltammetry, linear sweep voltammetry, impedance analysis, and chronoamperometry. Fig. 4(a) shows the cyclic voltammograms of NiO and Ni_2O_3 in 1 M KOH containing 0.150 M urea acquired at a scan rate of 10 mV s^{-1}. Despite having an equal onset oxidation potential value of the UOR at 0.34 V, the peak current density for Ni_2O_3 (36.32 mA cm^{-2}) is almost six times higher than that of NiO (5.94 mA cm^{-2}), revealing the higher activity of the Ni_2O_3 catalyst towards the UOR. When the scan polarity is reversed, we observe an anodic current arising from the oxidation of reactive intermediates adsorbed on the catalyst surface (intermediates generated in the forward scan get adsorbed on the catalyst surface). The oxidation of intermediates during the reverse scan continues till 0.32 V but the electrochemical UOR starts at a higher potential of 0.34 V *vs.* $Ag/AgCl_{(sat.KCl)}$, resulting in a CV crossover. A similar CV crossover has been observed by Vedharathinam *et al.* for the UOR in alkaline electrolytes.[5] The Tafel slope was taken by plotting log(current density) *vs.* applied UOR potential. The obtained Tafel slope for NiO and Ni_2O_3 is 104 and 21 mV dec^{-1}. The significantly less value obtained for Ni_2O_3 indicates faster kinetics exhibited by Ni_2O_3 than NiO and further confirms the superior activity of Ni_2O_3 (Fig. 4(b)). The Tafel slope obtained for Ni_2O_3 is relatively less than the values reported for the UOR in recent literature.[26] A Tafel slope of 31 mV dec^{-1} is shown for a MOF-derived nickel nitride catalyst,[27] while 49 mV dec^{-1} is reported for a nickel phosphide nanoflake array.[28] Ding *et al.*[29] compared the activity of atomically thin $Ni(OH)_2$ nanoholes and nanomeshes towards the UOR. They obtained a Tafel slope of 80 mV dec^{-1} for the $Ni(OH)_2$ nanomesh and 231 mV dec^{-1} for $Ni(OH)_2$ nanoholes. Nickel oxide supported on activated carbon black showed a Tafel slope of 79.57 mV dec^{-1} as compared to nickel oxide supported on multiwalled carbon nanotubes (85.35 mV dec^{-1}), graphene (90.87 mV dec^{-1}), and graphite (116.08 mV dec^{-1}).[9] The above studies are all based on NiO, while our research shows that Ni_2O_3 is a potential catalyst for the UOR.

The CVs of both samples are acquired in 1 M KOH in the absence of urea to study the active species (NiO(OH)) formation leading to UOR catalysis. Fig. 4(c) shows redox peaks (A_1) at 0.45 V in the forward scan resulting from the oxidation of Ni^{2+} ($Ni(OH)_2$) to Ni^{3+} (NiO(OH)) and the cathodic peak (C_1) at 0.36 V belonging to the reduction of Ni^{3+} to Ni^{2+} in 1 M KOH solution.[30] Similarly, Ni_2O_3 gives an anodic peak (A_2) at 0.424 V with a higher current density and a cathodic peak (C_2) in the reverse

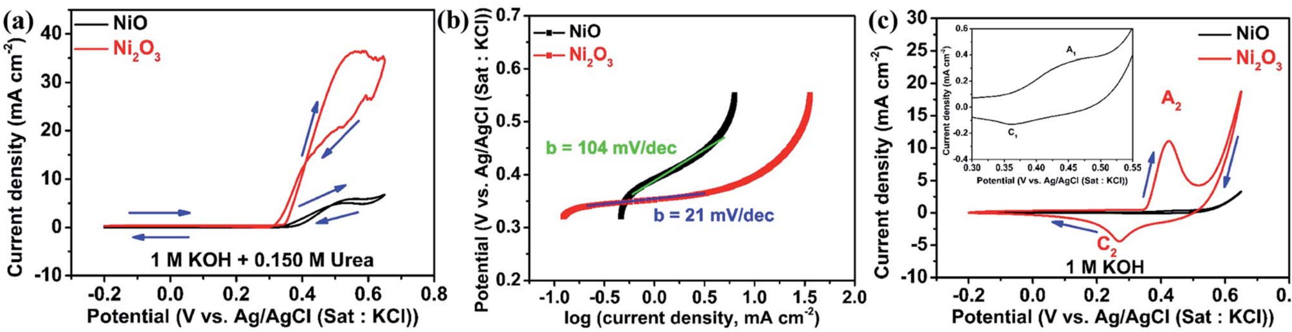

Fig. 4 (a) CV of NiO and Ni_2O_3 in 1 M KOH containing 0.150 M urea at a scan rate of 10 mV s^{-1}, (b) Tafel slope of NiO and Ni_2O_3 in 1 M KOH + 0.150 M urea, and (c) CV of NiO and Ni_2O_3 in 1 M KOH at a scan rate of 10 mV s^{-1} along with the magnified view of the redox region of NiO in the inset.

scan at 0.268 V. The anodic peak current density for Ni_2O_3 is 14 times higher as compared to NiO in 1 M KOH solution, which implies a greater number of oxidized Ni^{3+} ions that are significant active sites for the UOR. For a better comparison, the CVs of NiO and Ni_2O_3 in the presence (0.150 M urea) and absence of urea are shown in Fig. S5(a) and (b),† respectively. The electrochemical active surface area (ECSA) is calculated from double-layer capacitive current (C_{dl}), given in Fig. S6.† The Ni_2O_3 catalyst showed an ECSA of 0.74 cm^2, 2.5 times higher than that of NiO (0.29 cm^2). The higher ECSA value estimated for Ni_2O_3 also supports the improved UOR activity. The oxidized Ni^{3+} ions in Ni_2O_3 are more favorable for the adsorption of reactants, resulting in a high current for urea electro-oxidation. A detailed explanation is given below with theoretical modeling. The UOR performance is seen increasing with urea concentration in terms of current density achieved, and it shows a maximum in 0.150 M urea and 1 M KOH electrolyte solution. The effect of urea concentration on UOR performance is explained below.

Fig. 5(a) and (b) show the CV of NiO and Ni_2O_3 catalysts in 1 M KOH with varying molar concentrations of urea at a scan rate of 10 mV s^{-1}. For the NiO sample, the anodic peak current density attributed to the UOR performance increases with urea concentration (0 M to 0.150 M urea) and gets saturated near 0.150 M of urea. This current density increment is due to the increased accessibility of urea molecules for oxidation near the working electrode. This behavior signifies that the UOR is a diffusion-limited process when the urea concentration is less than 0.150 M. At lower concentrations, the surface coverage of the urea molecule on the catalyst is lower and with gradual increment in urea concentration, the surface coverage is enhanced, contributing to increase in current density. Once the urea concentration reaches 0.150 M, the catalyst lacks OH^- ions on the electrode surface for Ni^{2+} to Ni^{3+} oxidation (active species for urea oxidation) and as a result, a saturation of UOR current is observed. This speculation is confirmed by performing the UOR in 0.150 M urea with varying KOH concentrations from 1 to 8 M. It is observed that the urea electro-oxidation current increases gradually and saturates near an electrolyte concentration of 6 M KOH containing 0.150 M urea for NiO as can be noticed in Fig. 5(c) and accordingly, the redox peak current improvement of Ni^{2+} to Ni^{3+} is also observed (Fig. 5(c)). Even though the anodic peak current density saturated at 6 M KOH containing 0.150 urea, the onset potential continued to decrease towards a favorable lower potential from 0.34 V to 0.26 V during the increase in KOH concentration from 1 to 8 M.

Ni_2O_3 also shows a similar UOR current improvement with the urea concentration to the case of NiO (Fig. 5(b)). The UOR current achieves saturation at a urea concentration of 0.150 M. However, the maximum current obtained is much higher in this case, 35.85 mA cm^{-2} for 0.150 M urea in 1 M KOH, which is only 5.5 mA cm^{-2} for NiO and supports the effective adsorption of reactants on Ni_2O_3. We have also increased KOH concentration (1 to 8 M) concerning fixed urea concentration to enhance the UOR current, similar to the case of the NiO sample. However, current reduction is observed in this case, as seen in Fig. 5(d). A detailed CV of GCEs modified with NiO and Ni_2O_3 at different scan rates in various concentrations of urea and KOH is given

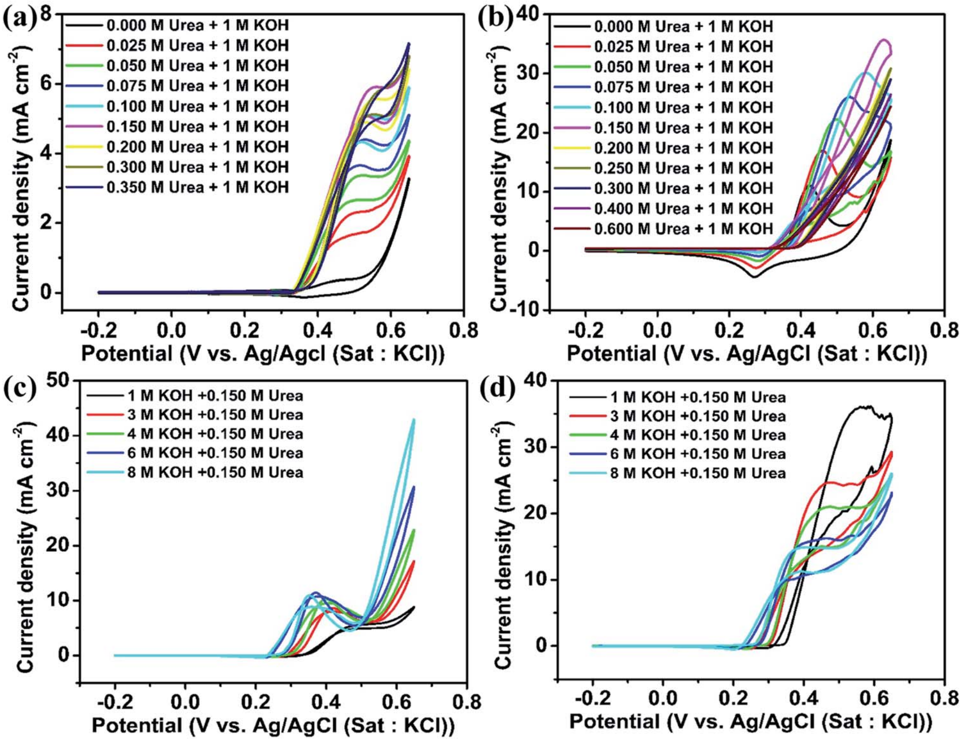

Fig. 5 CV of (a) NiO and (b) Ni_2O_3 modified GCEs in 1 M KOH containing various concentrations of urea: (c) NiO and (d) Ni_2O_3 in different molar concentrations of KOH with a fixed urea concentration of 0.150 M at a scan rate of 10 mV s^{-1}.

additionally (Fig. S7–S10†). Fig. S7 and S9† show the effect of urea concentration (in 1 M KOH) and the effect of KOH concentration (containing 0.150 M urea) for NiO, respectively, whereas Fig. S8 and S10† show the effect of urea concentration (in 1 M KOH) and effect of KOH concentration (containing 0.150 M urea) for Ni_2O_3, respectively.

In order to understand the UOR current reduction observed for Ni_2O_3 with increasing KOH, cyclic voltammetry is performed in 1 to 8 M KOH solutions in the absence of urea (Fig. S11†). The decrease in the anodic peak current density may arise due to $NiOO^-$ ion formation on the surface resulting from strong OH^- interaction at very high pH. Initially, 1 M KOH facilitated NiO(OH) formation *via* oxidation of surface species $Ni(OH)_2$ on Ni_2O_3. As the KOH concentration increases, the chemical deprotonation of the active species NiO(OH) forms a negatively charged species superoxide type $NiOO^-$ ions ($NiOOH + OH^- \rightarrow NiOO^- + H_2O$) that inhibit further OH^- adsorption.[31] As a result, a reduction in CV current with KOH concentration is observed. However, similar to what we observed for NiO, a decrease in onset potential towards a favorable direction is seen for Ni_2O_3 as well when the concentration of KOH is increased (0.34 V for 1 M KOH and 0.150 M urea to 0.25 V for 8 M KOH and 0.150 M urea).

Impedance analysis

Electrochemical impedance spectroscopy (EIS) is an efficient technique to study the number of electrochemical processes during the electrochemical reaction. The Nyquist plot is obtained by plotting real (Z') impedance *vs.* imaginary (Z'') impedance and gives information about solution resistance, and charge transfer resistances related to electrochemical reactions. In contrast, the Bode plot obtained by plotting log(frequency) *vs.* −phase angle gives details about the number of processes that occur during the electrochemical reaction.[32] For complex electrochemical reactions such as urea and methanol oxidation, the Nyquist plot with a negative real impedance value directly indicates the catalyst active site, which undergoes competitive phenomena such as surface poisoning by CO_x and its removal through OH^- ions that slow down the UOR.[33,34] Fig. 6(a) shows the Nyquist plot of the NiO catalyst at UOR potentials from 0.34 to 0.64 V in 1 M KOH containing 0.150 M urea. Initially, the impedance is monitored at 0.34 V *vs.* Ag/AgCl$_{(sat.KCl),}$ where the UOR starts. The spectra show a broad peak in the Nyquist plot that arises from the overlap of two small semicircles, which is identified through the appearance of two relaxation processes in the Bode plot (Fig. 6(c)). The higher frequency relaxation process ($10^{2.5}$ to $10^{1.9}$ Hz), as seen in the Bode plot, belongs to the Ni^{2+}/Ni^{3+} redox process and is related to an indirect UOR. Similarly, the occurrence of a low-frequency relaxation process near ($10^{1.7}$ to $10^{-0.90}$ Hz) represents direct urea electro-oxidation.[35–37] When the applied potential is increased gradually from 0.34 to 0.44 V (Fig. 6(a)), a reduction in the diameter of the two semicircles is observed. It can be seen in the enlarged plot given in Fig. 6(b). In the potential range of 0.34 to 0.44 V, all data points with positive real impedance values indicate CO_2 production as a rate-determining step for the UOR. At 0.48 V applied potential, the impedance data points in the low-frequency region undergo reversal with negative real impedance values ($10^{-0.50}$ to $10^{-2.0}$ Hz), and this behavior pertains till 0.52 V ($10^{0.42}$ to $10^{-2.0}$ Hz). The appearance of negative real impedance values is probably due to electrochemical surface oscillatory phenomena. This arises from competition between CO_x adsorption (blocks the active sites of the catalyst) and its removal by surface covered OH^- ions (release the blocked active sites) and makes CO_2 desorption a rate-determining step for the UOR.[33,34] The flip of impedance spectra (appearance of data points in II and III quadrants) with negative real impedance values is also reflected in the Bode plot as the −phase angle has values between ±90° to ±180° in the potential range 0.48 to 0.52 V (Fig. 6(c)) for NiO in 1 M KOH + 0.150 M urea. The flip of the impedance spectra explains that the catalyst is not poison tolerant. The produced CO_2 during urea electro-oxidation gets strongly adsorbed on the NiO surface without effective removal. As the potential increases from 0.56 to 0.64 V, the CO_2 production returns as the rate-determining step with positive real impedance values. Impedance analysis reveals CO_2 production as the rate-determining step at lower UOR potentials that alters to CO_2 desorption in the mid potential range (0.48 to 0.52 V). Finally, in the higher potential range, the CO_2 production returns as the rate-determining step. This behavior of NiO indicates that CO_2 surface poisons have a significant role in the electrochemical UOR and it is not entirely removed from the catalyst surface. The impedance spectra acquired in 3 M KOH + 0.150 M urea solution at various UOR potentials are shown in Fig. 6(d). It may be recalled from the CV (Fig. 5(c)) that the onset potential gets shifted to a lower potential value (0.30 V) with increase in KOH concentration. The impedance spectra of NiO in 3 M KOH + 0.150 M urea give positive real impedance values from 0.30 to 0.38 V, which change to negative real impedance values at 0.40 V ($10^{-0.83}$ to $10^{-2.0}$ Hz) remaining till 0.48 V ($10^{0.75}$ to $10^{-2.0}$ Hz). On further increasing the potential to 0.52 V (Fig. 6(e) and (f)), positive real impedance returns and is retained till 0.64 V. Fig. 6(g) shows the impedance spectra of NiO in 6 M KOH + 0.150 M urea. The positive real impedance values with CO_2 production as the rate-determining step are observed from 0.26 to 0.34 V and negative real impedance values with CO_2 desorption as a rate-determining step are observed from 0.36 ($10^{-0.25}$ to $10^{-0.20}$ Hz) to 0.44 V ($10^{0.67}$ to $10^{-0.20}$ Hz) (Fig. 6(i)). Further increase of potential from 0.48 to 0.64 V leads to CO_2 production as the rate-determining step with positive real impedance values (Fig. 6(h)). The shifting of the UOR onset potential and rate-determining step (CO_2 production and desorption) with KOH concentration is probably due to the concentration dependent potential shift[38] of the Ni^{2+}/Ni^{3+} redox (KOH concentration improves the pH of the electrolyte), which is confirmed by cyclic voltammetry of samples at various KOH concentrations (1 to 8 M) (Fig. 5(c) and S11†).

Ni_2O_3 impedance studies are carried out in 1 M KOH + 0.150 M urea solution at an initially applied potential of 0.34 V (onset potential for the UOR). The spectra show positive real impedance values from 0.34 to 0.44 V (Fig. 7(a)), which indicates CO_2 production as the rate-determining step and is confirmed by the

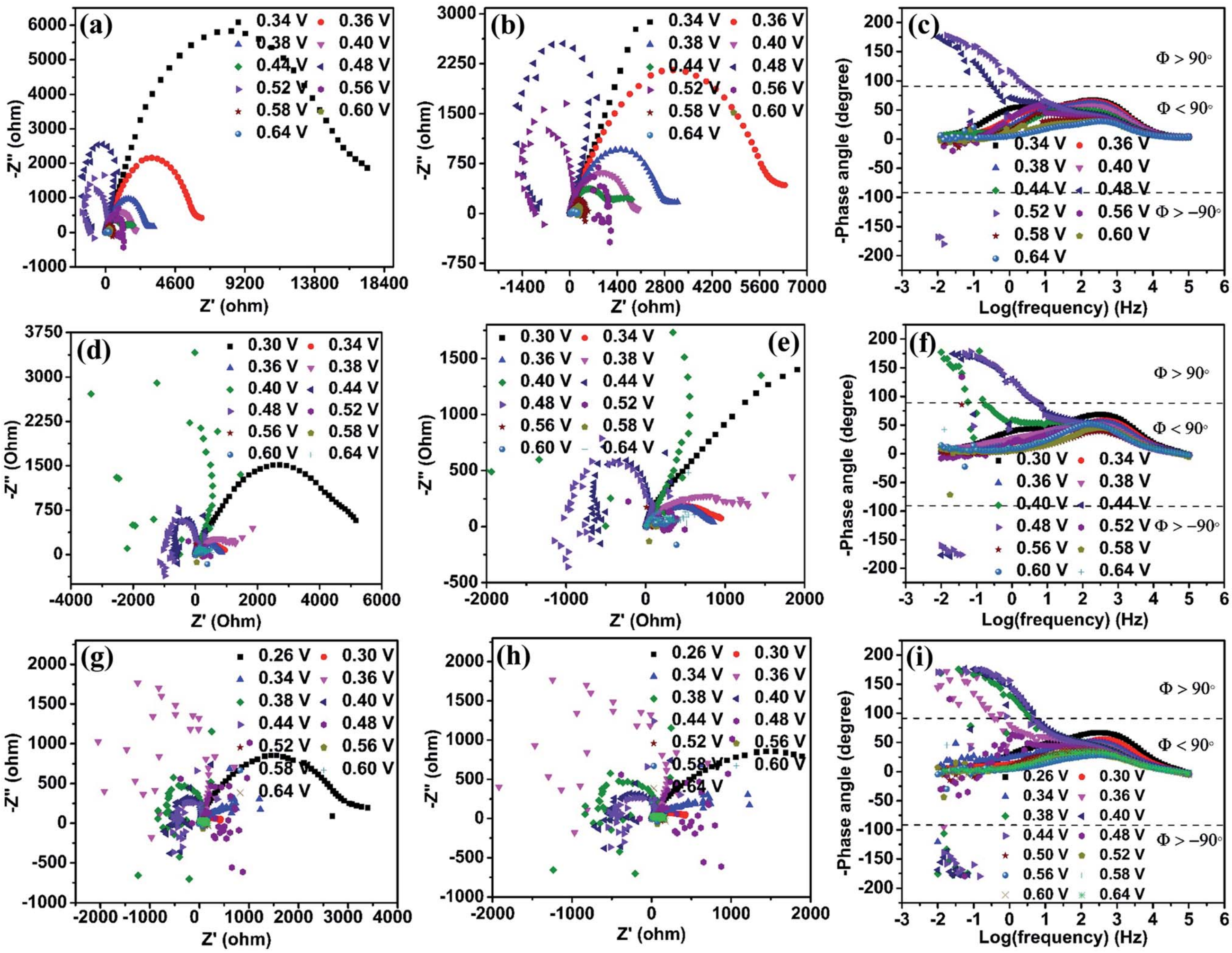

Fig. 6 Nyquist plots of the NiO catalyst in various electrolyte solutions: (a) 1 M KOH with 0.150 M urea, (d) 3 M KOH with 0.150 M urea and (g) 6 M KOH with 0.150 M urea. (b), (e) and (h) Zoomed-in view of the semicircle in the high-frequency region in (a), (d) and (g), respectively. Corresponding Bode plots of NiO in (c) 1 M KOH with 0.150 M urea, (f) 3 M KOH with 0.150 M urea and (i) 6 M KOH with 0.150 M urea.

Bode plot (−phase angle below 90°). When the applied potential is increased to 0.48 V, the impedance spectra start giving negative real impedance values (Fig. 7(b)), which appear in the frequency range of $10^{-1.5}$ to $10^{-2.0}$ Hz as observed from the Bode plot (−phase angle between ±90° and ±180°, Fig. 7(c)). In the case of Ni_2O_3, though the impedance data corresponding to the UOR potential range, 0.48 to 0.60 V, start giving negative real impedance, the data points are seen to vary between I and III quadrants. Accordingly, both negative and positive real impedance values are noted and might be taken as an indication of competition in the rate-determining step between CO_2 production and its desorption during the relaxation time between $10^{-1.5}$ to $10^{-2.0}$ Hz. The above may occur when competition between OH^- ions and CO_x for the active sites causes surface oscillatory behavior resulting in positive and negative real impedance in EIS. But once the surface is free from CO_x or in other words, if the catalyst is completely poison tolerant and active sites are covered/saturated by OH^- ions rather than CO_x, then positive real impedance should be observed. This can be achieved if the catalyst has weak adsorption for CO_2. To signify these processes (competition of CO_2 production and its desorption), we have counted the number of data points with negative real impedance values among the total points in those frequency ranges. The calculated points showing negative real impedance at a potential of 0.48 V from frequency $10^{-1.5}$ to $10^{-2.0}$ Hz are 6 out of 7, and further increasing potential to 0.50 V gives 4 out of 14 points in the frequency range of $10^{-0.92}$ to $10^{-2.0}$ Hz, 5 out of 14 points in the frequency range of $10^{-0.92}$ to $10^{-2.0}$ at 0.52 V, *etc.* (Table S4†). This is indicative of the high tolerance of the Ni_2O_3 catalyst against CO_x poisons.

In the case of NiO, the analysis of data points at 0.48 V in the frequency range of $10^{-0.50}$ to $10^{-2.0}$ Hz shows 18 continuous points out of 19 with negative real impedance under the same electrolyte conditions revealing that CO_2 production and its desorption competition is predominant for NiO. At increasing potential (0.52 V) for NiO, there is no significant difference in its impedance data behavior (Table S4†). These observations are supported by the Bode plot with the −phase angle varying between ±90° to ±180° (corresponding to Nyquist plot data

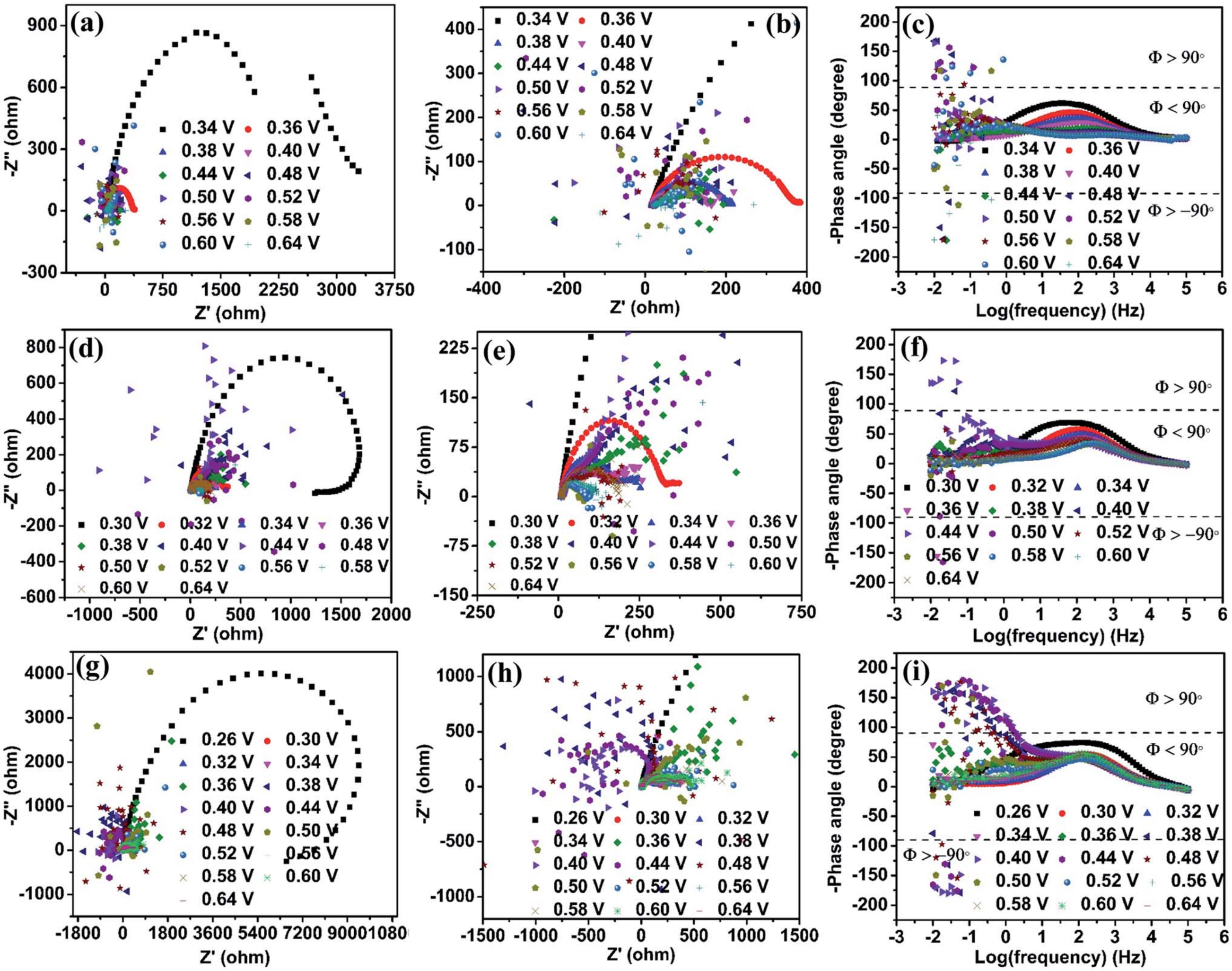

Fig. 7 Nyquist plots of the Ni_2O_3 catalyst in various electrolyte solutions: (a) 1 M KOH + 0.150 M urea, (d) 3 M KOH + 0.150 M urea and (g) 6 M KOH + 0.150 M urea. (b), (e) and (h) Enlarged views of the semicircle in the high-frequency region of (a), (d) and (g). Corresponding Bode plots in (c) 1 M KOH + 0.150 M urea, (f) 3 M KOH + 0.150 M urea and (i) 6 M KOH + 0.150 M urea.

points in negative real impedance values). This observation confirms that electrochemical oscillatory behavior is predominated by CO_2 poison in NiO and less in Ni_2O_3. The increase in KOH concentration till 3 M does not significantly change the impedance behavior for both the samples (Fig. 7(d)–(f)). The impedance data of Ni_2O_3 in 6 M KOH + 0.150 M urea at various UOR potentials show continuous negative real impedance data points similar to NiO as shown in Fig. 7(g) and (h) (20 out of 22) in the frequency range of $10^{-0.33}$ to $10^{-2.0}$ Hz at 0.38 V (Fig. 7(i)), and further increasing potential exhibits the same behavior as NiO. This might probably be due to the lack of OH^- coverage (confirmed by CV) and its availability on the Ni_2O_3 surface resulting in the equal number of surface adsorbed CO_2 and OH^- leading to surface oscillatory behavior[33] (Table S4†). The flipping of impedance data points with real impedance values from negative to positive is explained before and shown in Table S3.†

The data points with positive real impedance values are fitted considering the equivalent circuit in Fig. S12.† The R_s represents the solution resistance, and R_1 and CPE1 are the charge transfer resistance and constant phase elements for an indirect electrochemical UOR, while R_2 and CPE2 are the charge transfer resistance and constant phase elements for a direct electrochemical UOR.[39] The values of these fitted data are given in Table S5.† In 1 M KOH + 0.150 M urea solution, Ni_2O_3 shows comparatively lower charge transfer resistance for indirect ($R_1 = 5.171\ \Omega$) and direct ($R_2 = 3093\ \Omega$) reactions than NiO ($R_1 = 1049\ \Omega$ and $R_2 = 15\ 862\ \Omega$) indicating fast kinetics for the UOR, which is supported by the estimated low Tafel slope value. The impedance data points obtained for NiO and Ni_2O_3 at higher pH in 0.150 M urea + 3 M KOH and 6 M KOH solutions are also fitted using the equivalent circuit. The R_1 and R_2 values are seen reducing with increasing potential indicating a fast electrochemical UOR with applied potentials. It can be noticed that Ni_2O_3 shows lower resistance at all applied potentials than NiO for both direct and indirect reactions.

The electrochemical stability of both the catalysts during the UOR is studied using chronoamperometry in their respective

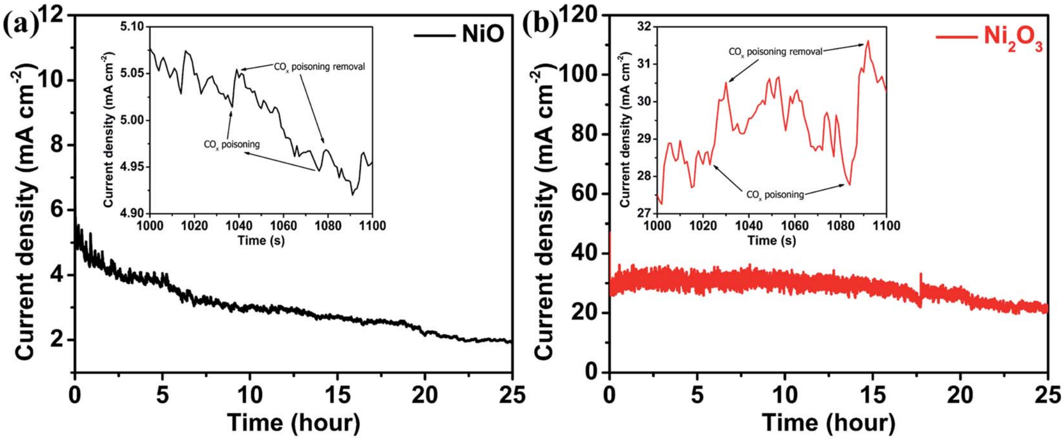

Fig. 8 *i–t* curves monitored for 25 hours for (a) NiO in 6 M KOH + 0.150 M urea at 0.40 V *vs.* Ag/AgCl$_{(sat.KCl)}$ and (b) the Ni_2O_3 catalyst in 1 M KOH + 0.150 M urea at 0.58 V *vs.* Ag/AgCl$_{(sat.KCl)}$; insets show the enlarged view of current density fluctuations.

electrolytes in which they exhibit high activity, 0.150 M urea + 1 M KOH for Ni_2O_3 and 0.150 M urea + 6 M KOH for NiO samples and at applied potentials at which the catalyst gives maximum current for the UOR, 0.40 and 0.58 V for NiO and Ni_2O_3, respectively. Stability studies of both samples are performed for 25 hours (Fig. 8). NiO shows an initial current density of 5.1 mA cm^{-2}, which reduced to 1.9 mA cm^{-2} after 25 hours (37% retention in current density). The up and down fluctuation of UOR current values indicates the blockage (reduction in current) and regeneration (current enhancement) of active sites (Fig. 8(a) and (b) inset). Fen Guo *et al.*[37] have shown that the current hike in *i–t* measurement is due to catalyst active site regeneration by OH^- ions and CO_x removal. They have also pointed out that the magnitude of current fluctuation increases with KOH concentration, implying that OH^- ions are effective in removing the poison from the catalyst surface. The magnitude of current fluctuation in the Ni_2O_3 sample (2.30 mA cm^{-2}) is higher than that of NiO (0.045 mA cm^{-2}), indicating effective CO_x poison removal with active site regeneration, supported by impedance spectra and complemented by the low Tafel slope value. Furthermore, effective active site regeneration and CO_x removal are the main factors in Ni_2O_3 for CO_x tolerance and sustained activity. The stability of Ni_2O_3 is compared with that of nickel oxide and hydroxide-based compounds available in the literature (Table S8†) and it shows that Ni_2O_3 is highly active for a longer duration of catalysis at a high current density (25 mA cm^{-2}). After the stability test (25 h), the Ni_2O_3 coating was scratched off from the GCE and washed several times with ethanol for TEM analysis to understand any structural and morphological change. The sheet-like morphology of Ni_2O_3 persists even after 25 h (Fig. S13†). Elemental mapping (Fig. S14†) and EDS analysis (Fig. S15†) also show the presence of nickel and oxygen. The above studies by LSV, CV, Tafel slope analysis, *i–t* curve analysis and EIS reveal that Ni_2O_3 is capable of generating efficient active species NiO(OH) and resultant high urea electro-oxidation current with significant CO_2 tolerance compared to NiO. In order to obtain more insights into the reaction mechanism as well as the activity difference exhibited by NiO and Ni_2O_3 surfaces towards the electrochemical urea oxidation reaction (UOR), we have performed DFT modeling. The adsorption energies of key reactants such as urea, hydroxyl, and CO_2 poison on the catalyst surface are calculated from the model.

Theoretical analysis on NiO and Ni_2O_3

DFT study has been performed based on *first-principles* calculations using the VASP simulation package.[40] As revealed by HRTEM analysis, the surface-exposed planes namely (111) and (002) of NiO and Ni_2O_3, respectively, are the active surfaces towards the electrochemical UOR. In this DFT study, both the Ni and O-terminated NiO (111) surfaces are considered, while Ni_2O_3 (002) can have only one stable surface termination as suggested by earlier studies.[41,42] The contribution from $Ni(OH)_2$ in Ni_2O_3 (002) was taken into account by hydrogenating a few Ni–O bonds in Ni_2O_3. However, as evident from experimental studies, under the influence of applied electrode potential in alkaline medium the catalyst surface will undergo surface reconstruction resulting in a hydroxylated active NiOOH surface before the UOR and this phenomenon is well explored in the literature.[11,43] Accordingly, we have constructed *in situ* generated dynamic hydroxylated surfaces and found out that the formation of a hydroxylated surface is more facile for Ni_2O_3 compared to NiO due to the presence of active Ni(III) centers on the Ni_2O_3 surface (Fig. S16†). The OH adsorption energies per OH species are −0.75 eV for the pristine NiO surface and −0.98 eV for the pristine Ni_2O_3 surface, indicating stronger OH adsorption on the Ni_2O_3 surface.

In a typical UOR process, the primary step is the adsorption of $CO(NH_2)_2$ (urea) on the surface of the electrocatalyst. Then the subsequent deprotonation of $CO(NH_2)_2$ occurs in an alkaline medium in the presence of OH^- ions resulting in CO_2 as the oxidized product.[11,43,44] The detailed mechanism of urea electro-oxidation is given in the ESI (Table S6†). However, as proposed earlier, the adsorption of $CO(NH_2)_2$ and desorption of CO_2 are the key processes in the electrochemical UOR.[11,43,44] The stronger the adsorption of $CO(NH_2)_2$, the higher will be the UOR

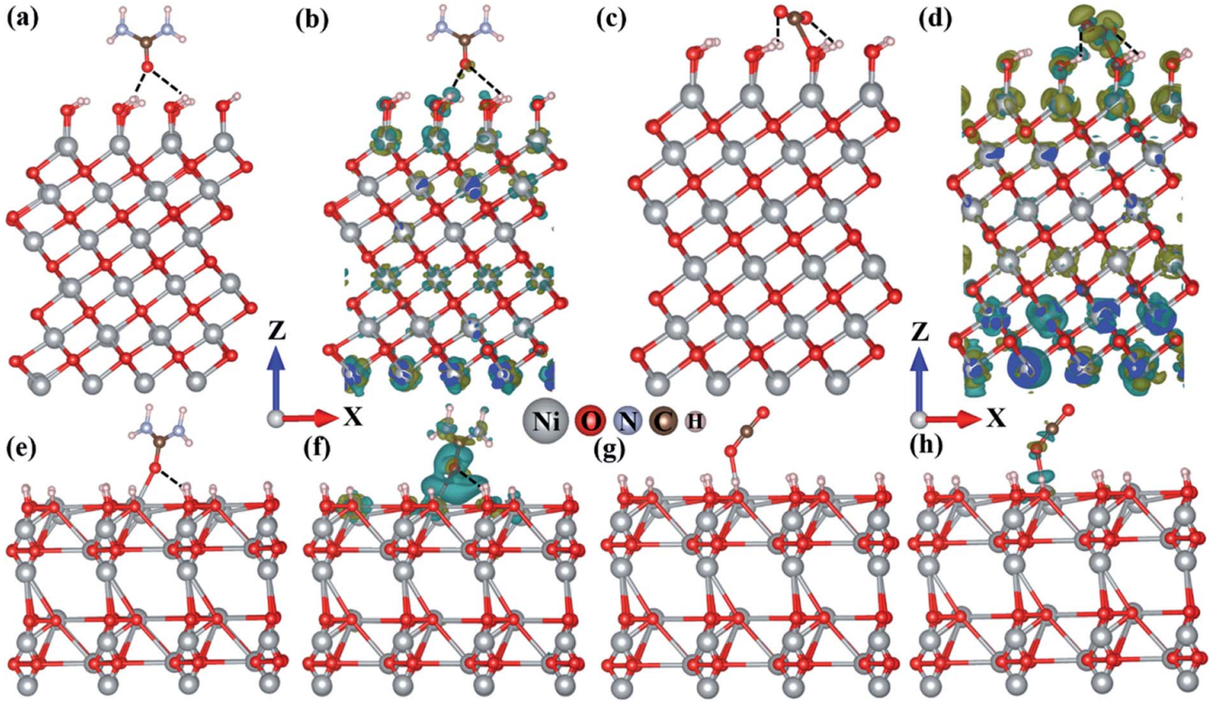

Fig. 9 Optimized structures and corresponding charge density difference (CDD) plots: (a and b) urea adsorbed, (c and d) CO_2 adsorbed Ni-terminated hydroxylated NiO (111) surface, (e and f) urea adsorbed, (g and h) CO_2 adsorbed hydroxylated Ni_2O_3 (002) surface. Isodensity value at surfaces is ±0.004 e a.u.$^{-3}$ (positive: cyan and negative: olive).

activity. According to DFT calculations, urea prefers to adsorb on the active hydroxylated Ni_2O_3 surface with an adsorption energy of −0.85 eV, while the adsorption energy on both the hydroxylated NiO (111) surfaces is −0.12 eV (Ni-termination) and −0.14 eV (O-termination) (Fig. 9 and S17†). Due to the unique surface structure of the hydroxylated Ni_2O_3 (002) surface, urea adsorbs on the Ni_2O_3 surface through strong covalent bonding interaction (between the Ni atom of the surface and the O atom of urea), while on hydroxylated NiO surfaces the adsorption occurs due to weak hydrogen bonding interactions resulting in stronger urea adsorption on the Ni_2O_3 surface. Besides adsorption energy, the stronger adsorption of urea on the Ni_2O_3 surface can also be rationalized through Bader charge population analysis and charge density difference (CDD) plots (Fig. 9 and S17†). Bader charge analysis quantifies that $0.18|e|$ charge is transferred from the Ni_2O_3 surface to urea, while merely $0.04|e|$ charge transfer occurred from the NiO surface to adsorbed urea, justifying stronger urea adsorption on Ni_2O_3. Bader charge analysis further supports CDD plots indicating enhanced charge transfer interaction and charge accumulation around the interacting region for the urea adsorbed Ni_2O_3 surface compared to the NiO surface.

Another important parameter for the electrochemical UOR is the facile desorption of CO_2 from the catalyst surface, which is considered the rate-limiting step for the UOR.[11,43,44] A weaker CO_2 adsorption is essential for an efficient UOR catalyst.[11,43,44] As evident from Fig. 9(c) and S17(c),† NiO surfaces strongly adsorb CO_2 through bonding interaction of the C atom of CO_2 and the O atom of hydroxylated surfaces as well as hydrogen bonding with an adsorption energy of −0.98 and −0.92 eV. The stronger adsorption of CO_2 can be vividly visualized from the bent structure of adsorbed CO_2. The linear CO_2 molecule (with $\angle$OCO angle 180° and C–O bond length 1.16 Å) bends to $\angle$OCO $= \sim 164°$ with the increase of the average C–O bond distance (1.22 Å) upon interaction with NiO surfaces, while relatively weaker adsorption of CO_2 (adsorption energy −0.45 eV) occurs on the Ni_2O_3 surface with bonding interaction with the O atom of CO_2 resulting in less bending of adsorbed CO_2 ($\angle$OCO $= \sim 178°$ and average C–O distance 1.17 Å). Moreover, Bader charge analysis and CDD plots further exhibit more charge transfer from the NiO surface ($0.16|e|$) to CO_2, while for Ni_2O_3 $0.07|e|$ charge is transferred (Fig. 9(d), (h) and S17(d)†). The adsorption energies of reactants and CO_2 for both the catalysts are compared in Table S7.† From this study, it can be envisaged that the Ni_2O_3 surface retards the CO_2 poisoning effect more efficiently compared to the NiO surface. Hence, based on two important factors namely the adsorption of urea and CO_2, it can be concluded that the Ni_2O_3 surface is superior to NiO for the electrochemical UOR with relatively stronger urea adsorption and weaker CO_2 adsorption ability.

Conclusions

This study projects Ni_2O_3 as a promising electrocatalyst for the urea oxidation reaction with its high activity and sustained urea oxidation reaction, which are correlated with the higher Ni^{3+}/Ni^{2+} active species formation, effective reactant adsorption, and better tolerance towards CO_2 poison. These are reflected in the observed higher UOR performance and lower Tafel slope for Ni_2O_3 compared to the conventional NiO catalyst at the same electrolyte concentration of urea and KOH. Detailed voltammetry and impedance studies are undertaken to get better insight into the catalyst activity and poison tolerance. A perfect reversal of impedance from the first quadrant to the second/third quadrants is observed for the NiO catalyst in a given applied potential window, implying that NiO is prone to CO_x poisoning to a large extent, while for the Ni_2O_3 catalyst, a complete reversal is not observed and this is an indication of CO_x tolerance in Ni_2O_3 as there is significant surface saturation by OH^- ions even in 1 M KOH. The surface saturation is associated with effective CO_x removal during the UOR and confirmed by cyclic voltammetry and impedance. A 70% UOR activity retention at a current density of 25 mA cm^{-2} for a 25 h duration is shown for Ni_2O_3, while the NiO catalyst can only retain 37% of the initial low current density for the same duration. The sustained UOR performance for Ni_2O_3 is due to better CO_x tolerance. Moreover, as gleaned from theoretical calculations, Ni_2O_3 has better reactant (urea and hydroxyl) adsorption as compared to NiO. At the same time, NiO has strong adsorption towards CO_2, which poisons the catalyst surface and affects its long-term activity. The Ni_2O_3 catalyst presents weaker adsorption to CO_2 facilitating better tolerance and prolonged UOR activity. This study provides a correlation between prominent hydroxylation and CO_x tolerance of the catalyst and gives insights into designing a UOR catalyst with optimum adsorption of reactants and poisons on its surface.

Conflicts of interest

There are no conflicts of interests to declare.

Acknowledgements

MS and CA thank CeNS for the research fellowship. The authors also thank CRF, CeNS for experimental facilities. The authors acknowledge MNIT, Jaipur for XPS analysis. R. J. thanks IACS and DST for research fellowship and A. D. thanks TRC-DST and SERB grant no. DIA/2018/000013 and CRG/2020/000301 for partial funding.

References

1 H. Zhou, F. Yu, Q. Zhu, J. Sun, F. Qin, L. Yu, J. Bao, Y. Yu, S. Chen and Z. Ren, *Energy Environ. Sci.*, 2018, **11**, 2858–2864.
2 X. Zou and Y. Zhang, *Chem. Soc. Rev.*, 2015, **44**, 5148–5180.
3 The United Nations World Water Development Report 2017. *Wastewater: the Untapped Resource*, UNESCO. Paris, 2017, vol. 53.
4 J. H. Meessen, *Urea in Ullmann's Encyclopedia of Industrial Chemistry*, 2010, DOI: 10.1002/14356007.a27_333.pub2.
5 V. Vedharathinam and G. G. Botte, *Electrochim. Acta*, 2013, **108**, 660–665.
6 V. Vedharathinam and G. G. Botte, *Electrochim. Acta*, 2012, **81**, 292–300.
7 G. Gnana, A. Farithkhan and A. Manthiram, *Adv. Energy Sustainable Res.*, 2020, **2000015**, 1–17.
8 F. Guo, K. Ye, K. Cheng, G. Wang and D. Cao, *J. Power Sources*, 2015, **278**, 562–568.
9 R. M. Abdel Hameed and S. S. Medany, *J. Colloid Interface Sci.*, 2018, **513**, 536–548.
10 H. M. Abd El-Lateef, M. M. Khalaf and I. M. A. Mohamed, *Ceram. Int.*, 2020, **46**, 20376–20384.
11 S. Lu, M. Hummel, Z. Gu, Y. Wang, K. Wang, R. Pathak, Y. Zhou, H. Jia, X. Qi, X. Zhao, B. Bin Xu and X. Liu, *ACS Sustainable Chem. Eng.*, 2021, **9**, 1703–1713.
12 Z. Yue, W. Zhu, Y. Li, Z. Wei, N. Hu, Y. Suo and J. Wang, *Inorg. Chem.*, 2018, **57**, 4693–4698.
13 B. Zhang, S. Wang, Z. Ma and Y. Qiu, *Appl. Surf. Sci.*, 2019, **496**, 143710.
14 L. Wang, S. Zhu, N. Marinkovic, S. Kattel, M. Shao, B. Yang and J. G. Chen, *Appl. Catal. B Environ.*, 2018, **232**, 365–370.
15 C. Alex, G. Shukla and N. S. John, *Electrochim. Acta*, 2021, **385**, 138425.
16 D. S. Hall, D. J. Lockwood, C. Bock and B. R. MacDougall, *Proc. R. Soc. A*, 2015, **471**, 20140792, DOI: 10.1098/rspa.2014.0792.
17 C. Li and S. Liu, *J. Nanomater.*, 2012, **1–6**, 648012, DOI: 10.1155/2012/648012.
18 S. Dey, S. Bhattacharjee, M. G. Chaudhuri, R. S. Bose, S. Halder and C. K. Ghosh, *RSC Adv.*, 2015, **5**, 54717–54726.
19 M. Fingerle, S. Tengeler, W. Calvet, T. Mayer and W. Jaegermann, *J. Electrochem. Soc.*, 2018, **165**, H3148–H3153.
20 R. E. Dietz, G. I. Parisot and A. E. Meixner, *J. Appl. Phys.*, 1971, **42**, 1484.
21 B. Zhao, X. K. Ke, J. H. Bao, C. L. Wang, L. Dong, Y. W. Chen and H. L. Chen, *J. Phys. Chem. C*, 2009, **113**, 14440–14447.
22 M. A. Peck and M. A. Langell, *Chem. Mater.*, 2012, **24**, 4483–4490.
23 A. F. Carley and S. Rassias, *Surf. Sci.*, 1983, **135**, 35–51.
24 H. A. E. Hagelin-Weaver, J. F. Weaver, G. B. Hoflund and G. N. Salaita, *J. Electron Spectrosc. Relat. Phenom.*, 2004, **134**, 139–171.
25 K. S. Kim and N. Winograd, *Surf. Sci.*, 1974, **43**, 625–643.
26 E. L. Ratcliff, J. Meyer, K. X. Steirer, A. Garcia, J. J. Berry, D. S. Ginley, D. C. Olson, A. Kahn and N. R. Armstrong, *Chem. Mater.*, 2011, **23**, 4988–5000.
27 S. Hu, S. Wang, C. Feng, H. Wu, J. Zhang and H. Mei, *ACS Sustainable Chem. Eng.*, 2020, **8**, 7414–7422.
28 D. Liu, T. Liu, L. Zhang, F. Qu, G. Du, A. M. Asiri and X. Sun, *J. Mater. Chem. A*, 2017, **5**, 3208–3213.
29 Y. Ding, Y. Li, Y. Xue, B. Miao, S. Li, Y. Jiang, X. Liu and Y. Chen, *Nanoscale*, 2019, **11**, 1058–1064.
30 B. K. Boggs, R. L. King and G. G. Botte, *Chem. Commun.*, 2009, 4859–4861.
31 O. Diaz-Morales, D. Ferrus-Suspedra and M. T. M. Koper, *Chem. Sci.*, 2016, **7**, 2639–2645.
32 S. M. Park and J. S. Yoo, *Anal. Chem.*, 2003, **75**, 455–461.
33 F. Seland, R. Tunold and D. A. Harrington, *Electrochim. Acta*, 2006, **51**, 3827–3840.

34 G. X. Cai, J. W. Guo, J. Wang and S. Li, *J. Power Sources*, 2015, **276**, 279–290.
35 I. M. A. Mohamed, P. Kanagaraj, A. S. Yasin, W. Iqbal and C. Liu, *J. Alloys Compd.*, 2020, **816**, 152513.
36 I. M. A. Mohamed and C. Liu, *Appl. Surf. Sci.*, 2019, **475**, 532–541.
37 F. Guo, K. Ye, M. Du, X. Huang, K. Cheng, G. Wang and D. Cao, *Electrochim. Acta*, 2016, **210**, 474–482.
38 G. Jerkiewicz, *ACS Catal.*, 2020, **10**, 8409–8417.
39 S. Qian, Z. Rao, Y. Liu, J. Yan, B. Fan, Y. Gui and F. Guo, *Electrochim. Acta*, 2020, **330**, 135211.
40 G. Kresse and J. Hafner, *Phys. Rev. B: Condens. Matter Mater. Phys.*, 1993, **47**, 558.
41 W. Zhao, M. Bajdich, S. Carey, A. Vojvodic, J. K. Nørskov and C. T. Campbell, *ACS Catal.*, 2016, **6**(11), 7377–7384.
42 W. B. Zhang and B. Y. Tang, *J. Chem. Phys.*, 2008, **128**, 124703.
43 S. Lu, M. Hummel, S. Kang, R. Pathak, W. He, X. Qi and Z. Gu, *ACS Omega*, 2021, **6**(22), 14648–14654.
44 Z. Ji, J. Liu, Y. Deng, S. Zhang, Z. Zhang, P. Du, Y. Zhao and X. Lu, *J. Mater. Chem. A*, 2020, **8**, 14680–14689.